communications physics

ARTICLE

https://doi.org/10.1038/s42005-022-00840-3 OPEN

Driving spin chirality by electron dynamics in laser-excited antiferromagnets

Sumit Ghosh [1✉], Frank Freimuth [1,2], Olena Gomonay [2], Stefan Blügel [1] & Yuriy Mokrousov [1,2]

Despite recent successes in the area of ultrafast manipulation of magnetic order, optical generation and manipulation of complex spin textures is hindered by an insufficient theoretical understanding of underlying processes. In particular an important aspect of subtle connection between the electronic and magnetic degrees of freedom is not properly accounted for in existing theories. Here, we uncover a distinct physical mechanism for imprinting spin chirality into collinear magnets with short laser pulses. By simultaneously treating the laser-ignited evolution of electronic structure and magnetic order, we show that their intertwined dynamics can result in an emergence of quasi-stable chiral states. We find that laser-driven chirality does not require any auxiliary external fields or intrinsic spin–orbit interaction to exist, and it can survive on the time scale of nanoseconds even in the presence of thermal fluctuations, which makes the uncovered mechanism relevant for understanding various optical experiments on magnetic materials. Our findings provide a more detailed perspective of the complex interactions which occur between chiral magnetism and light.

[1] Peter Grünberg Institut and Institute for Advanced Simulation, Forschungszentrum Jülich and JARA, 52425 Jülich, Germany. [2] Institute of Physics, Johannes Gutenberg-University Mainz, 55128 Mainz, Germany. ✉email: s.ghosh@fz-juelich.de

Chiral magnetic structures are perceived as indispensable components of the next generation of magnetic devices[1,2], and chirality itself emerges as a robust functional variable of magnetic systems[3–7]. The stabilisation of chiral magnetic states, such as spin-spirals[8], multi-q states[9], or skyrmions[10–12], has so far evolved predominantly along the lines of material and symmetry design of exchange interactions[13–15]. Application of continuous external electric and magnetic fields has also emerged as a powerful tool to induce chirality by the mechanism of symmetry-breaking[16] or current- and field-induced interactions[17–25]. Experimentally, localised chiral structures of various stability have been also produced by electromagnetic pulses[26], and in particular ultra-short laser pulses[27–29]. However, theoretical understanding of underlying mechanisms which drive chiral states in ultrafast experiments is rather unsatisfactory, as it mainly relies on the effective treatment of magnetisation dynamics which does not include electronic degrees of freedom into account explicitly[30–33]. While it is known that the laser-driven dynamics of electrons has a strong impact on the initial demagnetisation process[34–38], it is still not clear how electron dynamics, taking place on a much faster time scale, translates into the formation of large chiral magnetic states. Recent time-dependent density functional theory studies[39,40] have successfully captured microscopic effects like optically induced spin transfer, achieving good agreement with experimental findings, however, such studies are limited to sub-picosecond regime and they do not give any insight into longer relaxation mechanisms (~10 ps)[38] or formation of chiral magnetic order. Understanding these aspects is key, since it provides a direct link between electronic structure design and on-demand creation of macroscopic chiral magnetic objects with laser pulses.

In this work, we uncover a fundamental physical protocol for imprinting chirality in non-equilibrium spin systems. Taking one-dimensional antiferromagnetic chains as a platform, we explicitly consider the interaction between the electric field of the laser pulse with conduction electrons, which are in turn coupled to localised atomic spins, following the time-dependent coupled evolution of both sub-systems on equal footing. We thereby explicitly demonstrate that this intertwined dynamical process can result in a non-thermal formation of steady chiral states. We show that chirality formation is quite robust against the thermal fluctuations which make the uncovered mechanism relevant for various types of laser experiments performed on magnetic materials. Despite the simple model of the electronic structure we successfully capture the salient features of the underlying process emerging from the interplay between the electronic and magnetic interactions, thus providing a comprehensive strategy for an in-depth exploration of optically-driven chiral magnetism.

Results

Here, we focus on a simplified representative system—a one-dimensional antiferromagnetic (AFM) chain of N spins (see Fig. 1a) whose electronic properties are governed by the following double-exchange Hamiltonian[41–43] in presence of a laser field:

$$H(t) = -J \sum_{i;\mu,\nu} c^{\dagger}_{i,\mu} \left(\hat{\mathbf{M}}_i(t)\cdot\boldsymbol{\sigma}\right)_{\mu\nu} c_{i,\nu} - h \sum_{\langle i,j\rangle;\mu} c^{\dagger}_{i,\mu} c_{j,\mu} e^{\frac{ie}{\hbar}\mathbf{A}(t)\cdot\mathbf{d}_{ij}}. \quad (1)$$

where J denotes the strength of coupling between the local magnetic moment pointing along $\hat{\boldsymbol{M}}_i$ and the spin moment of a conduction electron. The value of J is kept at -1 eV resulting in an insulating gap of $2|J| = 2$ eV. Parameter h stands for the hopping amplitude and is kept at 0.4 eV. Note that the hopping takes place between the states of the same spin and thus the model does not possess any intrinsic spin-flip or spin–orbit coupling. The length of the chain is fixed to $N = 32$ sites. The

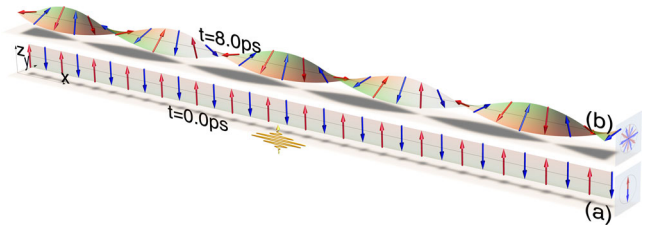

Fig. 1 Driving chiral antiferromagnetism by a short laser pulse. a Initial antiferromagnetic configuration in zx plane. Red and blue arrows represent initial up and down moments in the collinear antiferromagnetic ground state of the system. The yellow wavy line denotes the laser pulse polarised along the x-direction. **b** Following a complex intertwined dynamics of electrons and localised spins, a stable spin spiral state of the system is achieved (see Supplementary Movie 1 and Supplementary Note 2).

interaction of the laser pulse with the spin system is modelled by a Peierls substitution in the kinetic hopping, assuming that there is no absorption of angular momentum, which is found to have negligible impact on the magnetisation dynamics[44]. $\boldsymbol{A}(t)$ is the vector potential corresponding to the electric field of a Gaussian laser pulse $\mathcal{E}(t)$ given by

$$\mathcal{E}(t) = \mathcal{E}_0 \cos(\omega t) e^{-(t-t_0)^2/2s^2} \hat{\mathbf{x}}, \quad (2)$$

with angular frequency $\omega = 2.02|J|/\hbar = 3.07 \times 10^{15}$ Hz and a standard deviation $s = 5$ fs. The angular frequency is chosen to be slightly off-resonant from the bulk gap to maximise the absorption. The peak amplitude occurs at $t_0 = 100$ fs and it is chosen to be $\mathcal{E}_0 = 0.12\ \mathrm{V}.a_0^{-1}$ where a_0 is the inter-site distance (kept at the value of 1 in our calculations). For a lattice spacing of 2.4 Å it corresponds to a field strength of $5\ \mathrm{MV.cm}^{-1}$. We consider a linearly polarised pulse with polarisation along $\hat{x}$ axis and propagating along $\hat{z}$ axis (Fig. 1a).

The initial ground state is constructed by filling half of the eigenstates of H_0 which in our model are all the states with negative eigenvalues, the Fermi level remaining at zero energy. The magnetic ground state of this linear chain is antiferromagnetic[41] (see Supplementary Note 1). The quantum states $|\Psi_l(t)\rangle$ are evolved within time-dependent Schrödinger picture leading to an effective onsite magnetic field

$$\mathbf{B}_i(t) = \frac{1}{\mu_B} \sum_l \langle \Psi_l(t)| - \nabla_{\boldsymbol{M}_i} H(t) |\Psi_l(t)\rangle. \quad (3)$$

The field and the resulting torques $\boldsymbol{\tau}_i = \mu_B \hat{\boldsymbol{M}}_i \times \boldsymbol{B}_i$ are utilised to evolve magnetisation $\hat{\boldsymbol{M}}_i$ via a set of Landau–Lifshitz–Gilbert equations leading to hybrid quantum-classical dynamics of spins. For more information on the details of the method see section "Methods".

To describe the laser-excited spin and electron dynamics of the system we start with an initial AFM chain in zx plane (Fig. 1a). The effect of finite fluctuations is incorporated by adding small random polar ($\theta_{\mathrm{ran}} = 0.01$ rad) and azimuthal angle (ϕ randomly chosen between 0 and 2π) to each magnetisation direction. These small non-collinear components are imperative to initiate the dynamics. To describe the time evolution, we consider one specific random configuration (Fig. 1, Supplementary Note 2, and Supplementary Movie 1), while the averaged behaviour is discussed in Supplementary Note 3.

The dynamics of the system can be roughly divided into three different time regimes (vertical grey lines in Fig. 2) marked by the incident of the laser ($t_0 = 0.1$ ps), onset of magnetisation dynamics ($t_1 = 0.15$ ps) and the onset of the slow relaxation ($t_2 = 0.8$ ps). In the first regime ($t_0 < t < t_1$) the occupation of different quantum states changes instantly (Fig. 2a) without any change in the magnetisation (Fig. 2b). The mixing of quantum

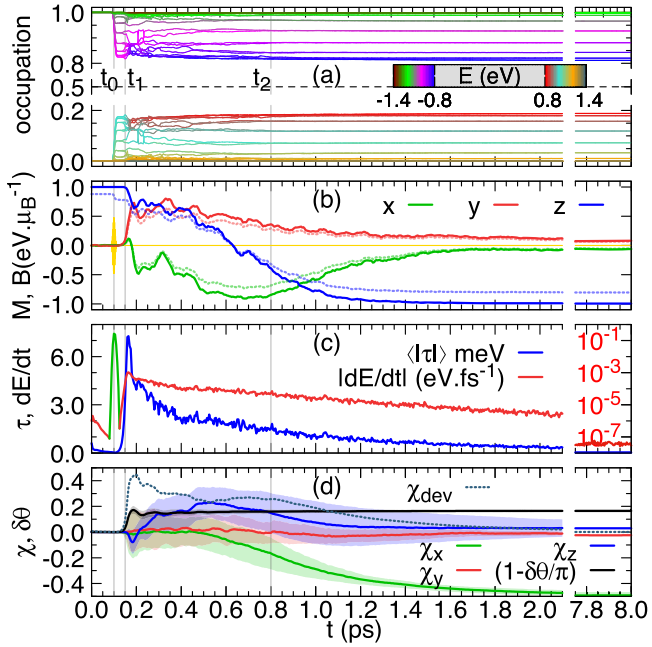

Fig. 2 Evolution of electron and spin subsystems over time. The laser hits at $t = t_0$, the magnetisation dynamics starts at $t = t_1$ and the slow relaxation dynamics starts at $t = t_2$. **a** Occupation of electronic states over time at half filling. The colours correspond to the eigenvalues (shown in inset). The black dashed line shows the average occupation which remains at 0.5. **b** Time evolution of magnetisation $\hat{\mathbf{M}}$ (solid) and effective field $\mathbf{B}$ (transparent, dotted) for 17th site. Yellow line denotes the laser pulse. **c** Average magnitude of the torque ($\langle|\boldsymbol{\tau}|\rangle = 1/N\sum_i^N |\mu_B \hat{\mathbf{M}}_i \times \mathbf{B}_i|$ in blue, scale on the left) and rate of change of energy (dE/dt, $\log_{10}$ scale on the right). Green and red colours correspond absorption and dissipation of energy. **d** Evolution of average chirality components and relative angle over time. The shaded regions show the root mean square deviation.

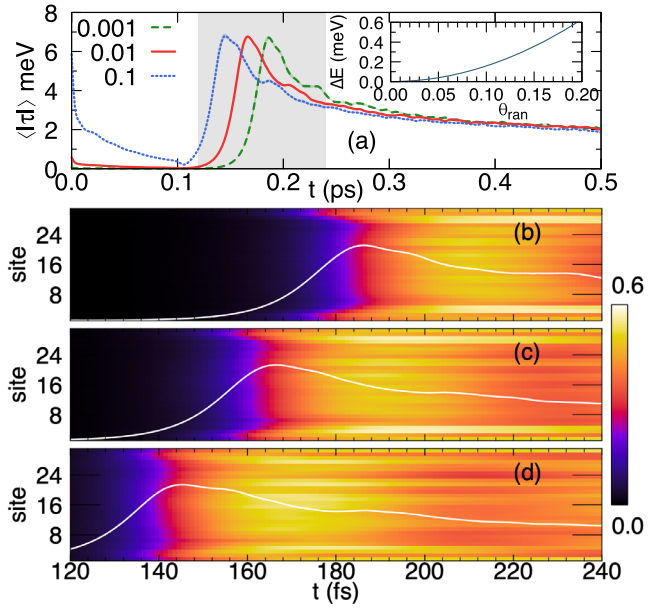

Fig. 3 Impact of randomness and edge effect on chiral formation. a Variation of effective torque as a function of initial randomness. Inset shows the average additional energy gain due to the randomness. Grey region denotes time span for which average chirality is calculated in (**b**–**d**). Evolution of magnitude of local chirality $|\chi_i|$ for an initial randomness (**b**) 0.001, (**c**) 0.01, and (**d**) 0.1. The plots show the distribution averaged over 64 different initial configurations. The white lines show the variation of $\langle|\tau|\rangle$ shown in (**a**).

states causes a change in the onsite $\mathbf{B}_i$ for the components parallel to the $\mathbf{M}_i$ only (Fig. 2b). Being stimulated by the initial random non-collinear components, the torques starts building up around $t \sim t_1$ (see Supplementary Note 2). A stronger randomness causes a faster response (Fig. 3 and Supplementary Note 3). In absence of any external stimulus, the system would eventually go back to its AFM ground state which is reflected in initial energy dissipation and reduction of effective torque (Fig. 2c).

In the second regime ($t_1 < t < t_2$) the system reorganises itself (see Supplementary Note 2). The quantum states strongly mix with each other (Fig. 2a) driving a significant change in the torques (Fig. 2c) and the orientation of magnetic moments (Fig. 2b). The overall duration of this process is of the order of that typical for laser-induced demagnetisation[38], which ensures that our model correctly captures the governing interactions between the laser field and magnetic moments. After that the system enters into the third regime ($t > t_2$) where the changes becomes much slower. At $t \sim 2$ ps, which is the same order as the reorientation time for ultrafast demagnetisation as well[38], the system has achieved its steady chiral state which survives on the time scale of several picoseconds (Figs. 1b). Note that at 8 ps, the system is dissipating energy at approximately 10^{-7} eV fs^{-1}. Considering the energy gain from the laser to be of the order of eV, the system can dissipate the additional energy on the nanosecond scale and come back to its initial ground state. It is worth mentioning that the Gilbert damping is not the only source of energy dissipation. The interaction between different quantum states can further modify the dissipation channel and consequently the dissipation rate is not simply proportional to the damping parameter only (Supplementary Note 4).

Chirality and relative angle. To characterise the evolution qualitatively, we define the average vector chirality $\boldsymbol{\chi} = \frac{1}{N-1}\sum_{i=1}^{N-1} \hat{\mathbf{M}}_i \times \hat{\mathbf{M}}_{i+1}$ and angular deviation $\delta\theta = \frac{1}{N-1}\sum_{i=1}^{N-1} \cos^{-1}(\hat{\mathbf{M}}_i \cdot \hat{\mathbf{M}}_{i+1})$, and evaluate these quantities over time for the chosen initial state (Fig. 2d). Since we are starting from an initial anti-ferromagnetic state, in the following we present the normalised angular deviation $1 - \delta\theta/\pi$ which is zero for a perfect antiferromagnet. The *perfection* of the state is quantified by the spiral deviation factor $\chi_{\mathrm{dev}} = \left|\sin(\delta\theta) - |\chi|\right|$, which is zero for a perfect spiral. One can readily see that the chirality components and angular deviation follow the same profile as the torque. For $t > t_2$ they converge to their asymptotic value with a decreasing root mean square deviation indicating an onset of the uniform spiral. This is further confirmed by the vanishing magnitude of χ_{dev}. Since $\delta\theta$ relies on the relative orientation of the adjacent sites only, it saturates much faster. It takes much longer, on the other hand, to establish and saturate an averaged chirality. The mechanism can be seen as a result of out-of-equilibrium chiral interactions such as Rashba–Bychkov interaction leading to asymmetric exchange interaction like DMI[45,46]. The saturation time of these entities depends on different system parameters, with their qualitative behaviour remaining similar.

Initial random orientation and edge effect. There are two driving factors that initiate the spiral formation. First is the initial randomness of magnetic orientation, which provides the initial non-chiral spin mixing interaction and thus ignites the magnetisation dynamics. In absence of any intrinsic spin-mixing interaction such as spin–orbit coupling, the magnetisation dynamics cannot be ignited without a small non-collinear magnetic component. A stronger randomness promotes more mixing which results in a faster build-up of effective torque (Fig. 3a) when compared to the case with smaller randomness. This behaviour is consistent with the time-dependent density

functional theory-based finding of ultrafast demagnetisation[44] where a stronger randomness results in a faster demagnetisation. As described in introduction, the randomness is introduced as a small random polar angle $\theta_{\rm ran}$ which pushes the system away from its actual ground state. This is reflected in the total energy of the system (Fig. 3a, inset). Initially, the system tries to come back to its true collinear ground state which is noticeable in the initial decrease in the torque (Fig. 3a). After being hit by the laser pulse at 0.1ps, the consequent mixing of quantum states causes a build up in torques (Fig. 3a) and initiates the magnetisation dynamics which is reflected in the rising magnitude of the average chirality (Fig. 3b–d). In pace with the torques the build up of chirality is also intensified by stronger randomness. Note that while the evolution of individual components of chirality can be different for different initial configurations, their magnitudes show a common trend which demonstrates the impact of the edges as the second governing factor. The edges act as a source of inversion symmetry breaking and thus can promote a dominant component of chirality as well (see Supplementary Note 5). The pivotal role of the edges is also reflected in the fact that the spiralisation starts at the edges—an effect that is more pronounced for smaller randomness (Fig. 3b–d). For larger randomness, the spiralisation on the average can initiate from any part of the system.

It is worth mentioning that in the present study we are not considering any structural defects of the underlying lattice. Such defects can give rise to new features in the optical response of a system and can play a vital role in the outcome of any photo-induced experiment. In one dimension, the presence of defects can be of crucial importance for the establishment of chiral coherence and dynamics of chirality nucleation along the chain, via the effect similar to that of the edges, where the changes in local environment can promote a faster build up of specific chirality. In higher dimensions, we believe that various types of defects can be exploited in a similar fashion to nucleate domains of specific chirality with optical pulses, in a way similar to that of defect or edge-assisted skyrmion nucleation with currents or pulses of magnetic field.

Chiral spin mixing interaction. Traditionally, the emergence of chirality is attributed to some sort of chiral spin mixing interaction (CSMI) (e.g., of Rashba–Bychkov type) leading to an antisymmetric exchange interaction (e.g., of DMI type). While our model itself does not possess any kind of CSMI intrinsically, the mixing of quantum states can give rise to an emergent CSMI. Similar mechanism is widely adopted in simulating SOC effect with ultra cold atoms[47,48]. In the latter case, very few quantum states are manipulated with a monochromatic laser which makes it possible to manipulate the exact form of the SOC[49]. In contrast to that, in our case, many more quantum states are involved and they are stimulated by a short pulse which excites many transitions as observed in the change of occupation of different quantum states (Fig. 2a). To validate the existence of any emergent CSMI we consider the most generic form of staggered (since we are considering antiferromagnetic configuration) chiral spin-mixing Hamiltonian, given by $H^r_\lambda = \sum_{\langle jk\rangle}(-1)^j(\mathrm{i}c^\dagger_j\sigma_r c_k - \mathrm{i}c^\dagger_k\sigma_r c_j)$ for $r = x, y, z$. Note that for our linear chain H^y_λ defines a staggered Rashba–Bychkov interaction which generates the y component of DMI. For our finite chain we define the instantaneous chiral spin-mixing strength as $\lambda_r(t) = \sum_l \langle\Psi_l(t)|H^r_\lambda|\Psi_l(t)\rangle/N$ and evaluate it over time.

To characterise the effective contribution of these interactions we define the integrated chiral strength as $\lambda^{\rm int}_r(t) = \int_t^{t_s}|\lambda_r(t')|\mathrm{d}t'$, where t_s corresponds to the time when the system reaches its steady state (8 ps in our case). To clarify our point, we consider three different initial configurations where the x, y, or z component of $\boldsymbol{\chi}$ dominates in the steady state (green, blue and red lines in Fig. 4a–c) and (compare corresponding $\lambda^{\rm int}_r(t)$ 4d–f). For brevity, in Fig. 4 we show the evolution of the latter quantity within 0.8–2 ps when the initial turbulence is over and the system starts moving towards its final configuration. One can readily see that the components of both $\boldsymbol{\chi}$ and $\lambda^{\rm int}$ show the same trend. For example, both in Fig. 4a–d the x components gradually become dominant while the other two components remains close. In Fig. 4b, e the y component is larger while Fig. 4c, f is marked by a dominant z component. The correspondence between the components of effective $\lambda^{\rm int}$ and that of the chirality, therefore, establishes the emergent CSMI as the source of the induced chirality. The emergent CSMI can be thus considered as the source of an out-of-equilibrium type of anti-symmetric exchange interaction, such as the Dzyaloshinskii–Moriya interaction, leading to a spiral in accord with equilibrium scenario[50,51]. Due to the random nature of the initial states, the system can promote any random combination of emergent interactions leading to any random end chirality. A preference can arise from the initial magnetic polarisation which can cause a particular combination of quantum states to appear in abundance. Further preference can be exerted by initially introducing a small spin-dependent hopping of Dresselhaus or Rashba–Bychkov type, which can maximise a particular flavour of mixing resulting in a specific end chirality (see Supplementary Note 5). Tuning the initial polarisation and spin-dependent hoping thus provides a controllable way to manipulate the end configuration.

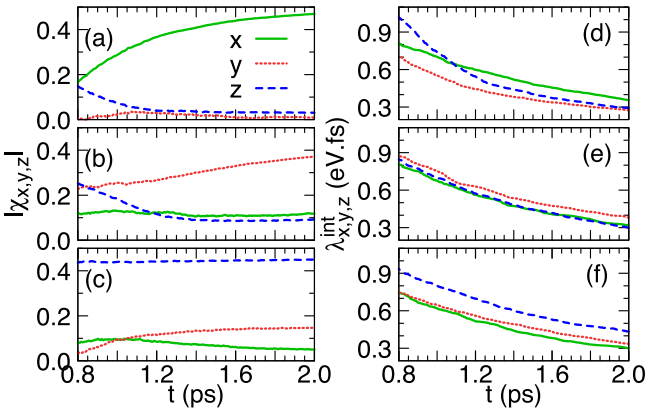

Fig. 4 Correlation between the components of vector chirality $\boldsymbol{\chi}$ and integrated chiral spin mixing interaction strength $\boldsymbol{\lambda}^{\rm int}$ for different initial configuration. a–c Show the evolution of components of $\boldsymbol{\chi}$ and **d–f** show the corresponding evolution of $\boldsymbol{\lambda}^{\rm int}$ for three different initial configurations. **a**, **d** Correspond the configuration considered in Figs. 1, 2. **b**, **e** and **c**, **f** Show the correlation for two other initial configurations . The green, blue and red lines in **a–c** show the magnitude of $\chi_{x,y,z}$ and in **d–f** they show the values of $\lambda^{\rm int}_{x,y,z}$.

Dependence on laser pulse intensity. A natural question arises whether it is possible to manipulate the degree of chirality in the system. In absence of any bias we characterise a spiral with $|\chi|$ and $\delta\theta$ and the deviation from a perfect spiral is given by the quantity $\chi_{\rm dev}$. From Fig. 5a, b, one can see that both $\delta\theta$ and $|\chi|$ pick up a finite value after a threshold field strength, which in turn correlates with the onset of the torque (Fig. 5c), and decreases with the increase in hopping parameter which facilitates strong overlap between sites. Note that even before the threshold the system absorbs energy from the pulse (Fig. 5d), which is invested into electronic transitions across the gap and changes quadratically with the pulse strength ($\mathcal{E}_0$). After the threshold, the pumped energy is also partly utilised for forming chirality, which results in

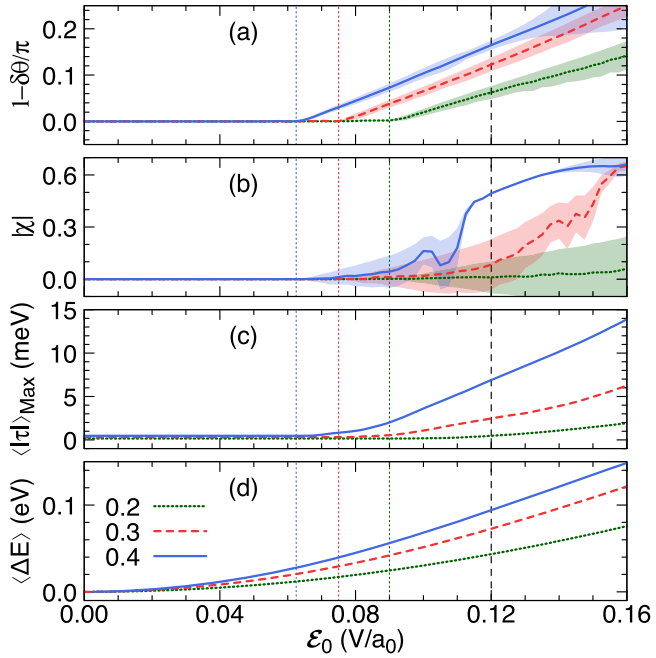

Fig. 5 Variation of different observables with respect to applied field strength for different hopping parameters. Variation of (**a**) relative angle $\delta\theta$, with the root mean square deviation given by shaded region; **b** chirality $|\chi|$, with shaded region denoting the χ_{dev}; **c** maximum average torque $\langle|\tau|\rangle_{Max}$, and (**d**) average pumped energy $\langle\Delta E\rangle$ with respect to the amplitude of the applied pulse $\mathcal{E}_0$. Green, red and blue lines represent hopping parameters 0.2, 0.3, and 0.4 eV and corresponding onset of $\delta\theta$ is denoted by the vertical dashed line of same colour. The values are averaged over 16 different configurations at 8 ps. The vertical black dashed line corresponds electric field used in Fig. 2.

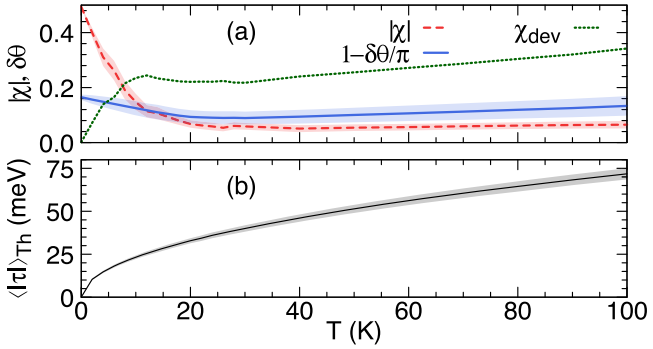

Fig. 6 Effect of ambient temperature on the chirality of the final configuration. Variation of (**a**) chirality (χ in red), relative angle ($\delta\theta$ in blue), χ_{dev} (green) and (**b**) average thermal torque, $\langle|\tau|\rangle_{Th}$ (root mean square deviation as shaded region), with temperature, for hopping parameter of 0.4 eV. The values are obtained at 8 ps from averaging over 64 configurations over a time period of 50 fs.

a deviation from the quadratic nature of the dispersion (Fig. 5d). Close to the threshold, large values of χ_{dev}, Fig. 5b, suggest that although the adjacent local magnetic moments are having a uniform angular deviation, the overall structure lacks global spiral order. Away from the threshold, the chain forms a steady spiral as marked by the vanishing χ_{dev}. For much stronger pulse intensities the system deviates from the steady spiral state again. This is due to the fact that a pulse with higher amplitude pumps more energy and the system requires more time to attain its smooth spiral configuration for fixed damping constant. Similar behaviour is observed with an increase of duration of the pulse or the frequency of the laser (see Supplementary Note 6).

Ambient temperature. We finally address the effect of ambient temperature on the stability of the laser-driven spiral states, which in our calculations is introduced as an additional time-dependent onsite random field $\boldsymbol{B}_i^{\mathrm{Th}}(t) = \sqrt{(2\alpha k_B T\mu_i/\gamma\delta t)}\boldsymbol{\eta}_i(t)$, where each component of $\boldsymbol{\eta}(t)$ follows a normal distribution over the sites at each time[52]. Considering the small system size, this approach may lead to an overestimation of thermal effects. Due to the large (2 eV) gap, the ambient temperature range under consideration would not cause any change in electronic occupation. With increasing T, chirality decreases rapidly away from its "ideal" value, whereas the angular deviation exhibits a very robust behaviour (Fig. 6a and Supplementary Note 7). However, chirality does not vanish entirely but rather saturates at a residual value, although the magnitude of χ_{dev} indicates that the resulting state is far from being a perfect spiral. We note that the torque due to the thermal fluctuations, Fig. 6b, does not depend on model parameters, whereas the effective field and corresponding torque do (Fig. 5c). Therefore it might be possible to reduce the thermal impact by tuning the system parameters.

Discussion

In our work, we introduce an alternative paradigm to imprint chirality in magnets with a finite laser pulse. Our results show that the laser-driven magnetisation dynamics is preceded by the electronic excitation with a lag time depending on the initial magnetic configuration. By establishing a bridge between the quantum evolution of electronic states and classical spin dynamics, we present a comprehensive picture of the laser-mediated formation of large-scale chiral states. We highlight that the uncovered mechanism is distinctly different from that which is commonly used to interpret laser excited dynamics in terms of transfer of effective temperature between electronic to spin degrees of freedom which is also known as two temperature or three temperature model (considering the phonon modes)[53,54]. Although these phenomenological models work nicely for ultrafast demagnetisation, they fail to capture the physics of ultrafast generation of chirality.

To show this, we artificially simulate the effect of heating of the electronic sub-system. Due to the presence of a large gap and the fact that the laser pulse only changes the occupation of a small range of eigenstates within a specific energy window, it is not possible to construct a thermal distribution to capture these phenomena. Therefore we replace the laser with a change of occupation by hand at time t_0 (Fig. 7a) with a random phase factor to simulate the effect of thermal transition and let the system evolve (Fig. 7b). We observe that with thermal excitation the system forms multiple domains rather than a smooth spiral (Fig. 7c). In accord to existing knowledge, such formation can change the effective magnetic order which can be observed in experiments on ultrafast demagnetisation. However, the large root mean square deviation of $\delta\theta$ and large values of χ_{dev} (Fig. 7b) compared to laser-excited dynamics shows that the thermal excitation does not guide the system to a spiral formation. This has been further clarified by showing the end configuration of the evolution (Fig. 7c and Supplementary Note 8).

The approach used in our work successfully captures the salient features of the intertwined electronic and magnetic dynamics which is crucial in optical manipulation of chiral magnetic structures, and paves a way for further material design aimed at optimisation of time scales and energetics involved. The proposed paradigm also provides a fruitful ground for studying diverse effects related to the interplay of optical chiral dynamics

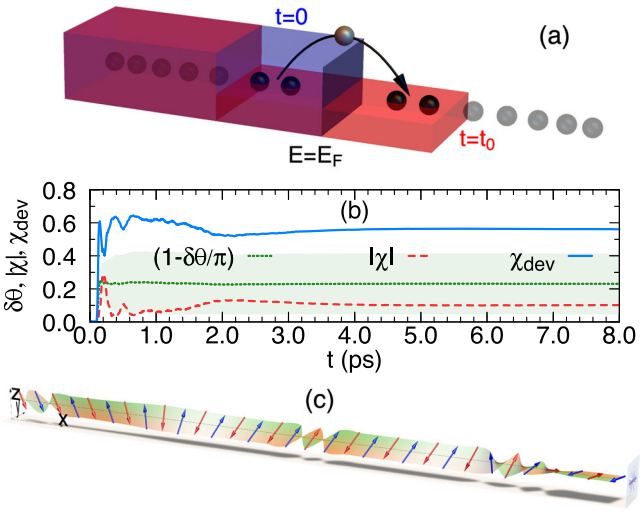

Fig. 7 Evolution of thermally initiated magnetisation dynamics. a Schematic of simulating thermal occupation. Blue and red regions show the occupation distribution at $t = 0$ and $t = t_0$ which is introduced to simulate the thermal impact of the laser. **b** Relative angle ($\delta\theta$), chirality ($|\chi|$) and chiral deviation (χ_{dev}) for a specific configuration. The shaded green region shows the root mean square deviation of $\delta\theta$. The excitation takes place at 0.1ps. **c** End configuration of the evolution at 8 ps.

with the effects of spin relaxation, impurity scattering and phonon excitations. The ability to take into account a large number of atoms as well as related spin and electronic dynamical effects can become indispensable for addressing the influence of chiral dynamics on demagnetisation processes[44], or optically assisted creation of exotic chiral particles such as hopfions[55]. Such versatility can be instrumental in exploring new possibilities of light–matter interaction in magnetic materials.

Methods

A linear chain with antiferromagnetic magnetic ordering can be represented with a tight binding Hamiltonian

$$H_0 = -J \sum_{i;\mu,\nu} c^{\dagger}_{i,\mu} \left(\hat{\mathbf{M}}_i \cdot \boldsymbol{\sigma}\right)_{\mu\nu} c_{i,\nu} - h \sum_{\langle i,j\rangle;\mu} c^{\dagger}_{i,\mu} c_{j,\mu}, \tag{4}$$

where $c_{i,\mu}$ and $c^{\dagger}_{i,\mu}$ stand for electron creation and annihilation operators at site i and spin component μ and $\langle i,j\rangle$ denotes all nearest neighbour pairs. $\boldsymbol{\sigma}$ is the vector of Pauli matrices, $\hat{\mathbf{M}}_i$ is the unit vector denoting the direction of magnetic moment at site i. J is the coupling strength between the local magnetic moment and the spin moment of a conduction electron and h is the hopping amplitude. We subject the system to the action of a laser pulse, which we model as a time-varying electric field in the form of a Gaussian:

$$\mathcal{E}(t) = \mathcal{E}_0 \cos(\omega t) \mathrm{e}^{-(t-t_0)^2/2s^2} \hat{\mathbf{x}}, \tag{5}$$

with angular frequency ω and a standard deviation s. We consider a linearly polarised pulse with polarisation along $\hat{x}$ axis and propagating along $\hat{z}$ axis. The impact of this electric field can be modelled as an Peierls phase $\mathrm{e}^{\frac{ie}{\hbar}\mathbf{A}(t)\cdot\mathbf{d}_{ij}}$ where $\boldsymbol{A}(t)$ is the time-dependent vector potential such that $\mathcal{E}(t) = -\partial \boldsymbol{A}(t)/\partial t$, e is the electronic charge and $\boldsymbol{d}_{ij}$ is the vector connecting site i to j. This results in the following time-dependent Hamiltonian

$$\begin{aligned} H(t) = &-J \sum_{i;\mu,\nu} c^{\dagger}_{i,\mu} \left(\hat{\mathbf{M}}_i(t) \cdot \boldsymbol{\sigma}\right)_{\mu\nu} c_{i,\nu} \\ &-h \sum_{\langle i,j\rangle;\mu} c^{\dagger}_{i,\mu} c_{j,\mu} \mathrm{e}^{\frac{ie}{\hbar}\mathbf{A}(t)\cdot\mathbf{d}_{ij}} \end{aligned} \tag{6}$$

The corresponding time evolution of the quantum states is evaluated in small time steps ($\delta t = 0.001$ fs). As magnetisation dynamics is a slower process as compared to the evolution of quantum states, the magnetic moments practically remain constant during each step of electronic evolution. In that case, the time evolution of the n'th instantaneous eigenstate $|\phi_n(t)\rangle$ of $H(t)$ reads $|\phi_n(t+\delta t)\rangle = \mathrm{e}^{-iH(t)\delta t/\hbar}|\phi_n(t)\rangle$. Any initial state can be expressed as a linear combination of these basis states and at any instance t the time evolution of any arbitrary state $|\Psi_l\rangle$ can be expressed as $|\Psi_l(t+\delta t)\rangle = \sum_n c^l_n(t)\mathrm{e}^{-iH(t)\delta t/\hbar}|\phi_n(t)\rangle$, where $c^l_n(t) = \langle\phi_n(t)|\Psi_l(t)\rangle$ is the instantaneous overlap integral subjected to the initial condition $c^l_n(0) = \delta_{nl}$. At half filling of an antiferromagnetic ground state, it populates all the states with negative eigenvalues. (Fig. 2a and Supplementary Note 2).

The quantum evolution of the states is coupled to the magnetisation dynamics of the chain as governed by a set of Landau–Lifshitz–Gilbert equations

$$\frac{\mathrm{d}\hat{\mathbf{M}}_i}{\mathrm{d}t} = -\gamma'[\hat{\mathbf{M}}_i \times \mathbf{B}_i(t)] - \lambda[\hat{\mathbf{M}}_i \times (\hat{\mathbf{M}}_i \times \mathbf{B}_i(t))], \tag{7}$$

where $\gamma' = \frac{\gamma}{1+\alpha^2}\frac{1}{\mu_i}$ and $\lambda = \frac{\gamma\alpha}{1+\alpha^2}\frac{1}{\mu_i}$ with $\gamma = \frac{g_e\mu_B}{\hbar}$, $g_e = 2$ is the gyromagnetic ratio, μ_B is Bohr magneton and μ_i is the magnetic moment at site i which we choose to be 1 μ_B on each site. α is the dimensionless damping parameter which we keep constant at a value of 0.2. The time-dependent onsite effective magnetic fields $\mathbf{B}_i(t)$ are given by

$$\mathbf{B}_i(t) = \frac{1}{\mu_B}\sum_l \langle\Psi_l(t)| - \nabla_{\mathbf{M}_i} H(t)|\Psi_l(t)\rangle. \tag{8}$$

By solving Eqs. (7) and (8) simultaneously we are thereby able to study the effect of the laser pulse on the magnetisation dynamics as mediated by excited electronic states. In the past, a similar approach has been adopted to study the quantum evolution of magnetic system[41–43] and current-driven magnetisation dynamics[56,57], however, a steady chirality formation was not observed. Ishihara and Ono[43] observe a transient skyrmion-like configuration during a periodically-driven laser-assisted transition from a ferromagnetic to an antiferromagnetic state, stable on the scale of hundred femtoseconds. Contrary to that, as discussed below, we observe the formation of steady chiral states which can survive up to several picoseconds and can be generated with a finite pulse.

One should note that the exact mechanism of energy dissipation in such driven system can be very complicated[58–60]. For simplicity, we do not include the effects of relaxation due to electron–electron, electron–phonon, or electron–magnon interaction explicitly, noting that they can be effectively incorporated via a suitable modification of the damping parameter[61,62]. The exact treatment of the electron excitation during the action of the laser pulse is important to compute the nonequilibrium spin polarisations that drive the system into the noncollinear state. We assume that once the nonequilibrium spin polarisations are present and the laser-pulse has been switched off, the exact energies of the conduction electrons are less important for the magnetisation dynamics, and therefore we assume that we may ignore the fast fs energetic relaxation of the electrons. In particular, we assume that the laser excites the conduction electrons to higher energies and to different spin expectation values and that the nonequilibrium spin expectation values persist to the ps time scale while only the energies of the excited electrons relax on the fs time scale.

Data availability

The data that support the findings of this study are available from the corresponding author upon reasonable request.

Received: 9 August 2021; Accepted: 17 February 2022;
Published online: 25 March 2022

References

1. Koshibae, W. et al. Memory functions of magnetic skyrmions. *Jpn. J. Appl. Phys.* **54**, 053001 (2015).
2. Lonsky, M. & Hoffmann, A. Dynamic excitations of chiral magnetic textures. *APL Mater.* **8**, 100903 (2020).
3. Menzel, M. et al. Information transfer by vector spin chirality in finite magnetic chains. *Phys. Rev. Lett.* **108**, 197204 (2012).
4. Li, X. et al. Chiral domain walls of Mn3Sn and their memory. *Nat. Commun.* **10**, 3021 (2019).
5. Balz, C. et al. Finite field regime for a quantum spin liquid in $RuCl_3$. *Phys. Rev. B* **100**, 060405 (2019).
6. Kerber, N. et al. Chiral versus collinear magnetic order dynamics: Faster chiral recovery after optical excitation revealed by femtosecond XUV scattering. *Nat. Commun.* **11**, 6304 (2020).
7. Leveille, C. et al. Ultrafast time-evolution of magnetic chirality probed by circular dichroism in X-ray resonant magnetic scattering in homochiral skyrmionic systems. Unpublished. Preprint at https://arxiv.org/abs/2007.08583 (2020).
8. Bode, M. et al. Chiral magnetic order at surfaces driven by inversion asymmetry. *Nature* **447**, 190–193 (2007).
9. Takagi, R. et al. Multiple- q noncollinear magnetism in an itinerant hexagonal magnet. *Sci. Adv.* **4**, eaau3402 (2018).
10. Sampaio, J., Cros, V., Rohart, S., Thiaville, A. & Fert, A. Nucleation, stability and current-induced motion of isolated magnetic skyrmions in nanostructures. *Nat. Nanotechnol.* **8**, 839–844 (2013).
11. Jiang, W. et al. Blowing magnetic skyrmion bubbles. *Science* **349**, 283–286 (2015).

12. Hirschberger, M. et al. Skyrmion phase and competing magnetic orders on a breathing kagomé lattice. *Nat. Commun.* **10**, 5831 (2019).
13. Dupé, B., Bihlmayer, G., Böttcher, M., Blügel, S. & Heinze, S. Engineering skyrmions in transition-metal multilayers for spintronics. *Nat. Commun.* **7**, 11779 (2016).
14. Grytsiuk, S. et al. Topological-chiral magnetic interactions driven by emergent orbital magnetism. *Nat. Commun.* **11**, 511 (2020).
15. Paul, S., Haldar, S., von Malottki, S. & Heinze, S. Role of higher-order exchange interactions for skyrmion stability. *Nat. Commun.* **11**, 4756 (2020).
16. Srivastava, T. et al. Large-voltage tuning of Dzyaloshinskii–Moriya interactions: A route toward dynamic control of skyrmion chirality. *Nano Lett.* **18**, 4871–4877 (2018).
17. Sato, M., Takayoshi, S. & Oka, T. Laser-driven multiferroics and ultrafast spin current generation. *Phys. Rev. Lett.* **117**, 147202 (2016).
18. Freimuth, F., Blügel, S. & Mokrousov, Y. Dynamical and current-induced Dzyaloshinskii–Moriya interaction: Role for damping, gyromagnetism, and current-induced torques in noncollinear magnets. *Phys. Rev. B* **102**, 245411 (2020).
19. Karnad, G. V. et al. Modification of Dzyaloshinskii–Moriya-interaction-stabilized domain wall chirality by driving currents. *Phys. Rev. Lett.* **121**, 147203 (2018).
20. Kato, N. et al. Current-induced modulation of the interfacial Dzyaloshinskii–Moriya interaction. *Phys. Rev. Lett.* **122**, 257205 (2019).
21. Yudin, D., Gulevich, D. R. & Titov, M. Light-induced anisotropic skyrmion and stripe phases in a Rashba ferromagnet. *Phys. Rev. Lett.* **119**, 147202 (2017).
22. Stepanov, E. A., Dutreix, C. & Katsnelson, M. I. Dynamical and reversible control of topological spin textures. *Phys. Rev. Lett.* **118**, 157201 (2017).
23. Lux, F. R., Freimuth, F., Blügel, S. & Mokrousov, Y. Engineering chiral and topological orbital magnetism of domain walls and skyrmions. *Commun. Phys.* **1**, 60 (2018).
24. Ishihara, S. Photoinduced ultrafast phenomena in correlated electron magnets. *J. Phys. Soc. Jpn.* **88**, 072001 (2019).
25. Boström, E. V., Rubio, A. & Verdozzi, C. Microscopic theory of ultrafast skyrmion excitation by light. Unpublished. Preprint at http://arxiv.org/abs/2010.16125 (2020).
26. Romming, N., Kubetzka, A., Hanneken, C., von Bergmann, K. & Wiesendanger, R. Field-dependent size and shape of single magnetic syrmions. *Phys. Rev. Lett.* **114**, 177203 (2015).
27. Finazzi, M. et al. Laser-induced magnetic nanostructures with tunable topological properties. *Phys. Rev. Lett.* **110**, 177205 (2013).
28. Je, S.-G. et al. Creation of magnetic skyrmion bubble lattices by ultrafast laser in ultrathin films. *Nano Lett.* **18**, 7362–7371 (2018).
29. Büttner, F. et al. Observation of fluctuation-mediated picosecond nucleation of a topological phase. *Nat. Mater.* **20**, 30–37 (2021).
30. Koshibae, W. & Nagaosa, N. Creation of skyrmions and antiskyrmions by local heating. *Nat. Commun.* **5**, 5148 (2014).
31. Fujita, H. & Sato, M. Ultrafast generation of skyrmionic defects with vortex beams: Printing laser profiles on magnets. *Phys. Rev. B* **95**, 054421 (2017).
32. Polyakov, O. P., Gonoskov, I. A., Stepanyuk, V. S. & Gross, E. K. U. Generation of magnetic skyrmions by focused vortex laser pulses. *J. Appl. Phys.* **127**, 073904 (2020).
33. Miyake, M. & Mochizuki, M. Creation of nanometric magnetic skyrmions by global application of circularly polarized microwave magnetic field. *Phys. Rev. B* **101**, 094419 (2020).
34. Kirilyuk, A., Kimel, A. V. & Rasing, T. Ultrafast optical manipulation of magnetic order. *Rev. Mod. Phys.* **82**, 2731–2784 (2010).
35. Krieger, K., Dewhurst, J. K., Elliott, P., Sharma, S. & Gross, E. K. Laser-induced demagnetization at ultrashort time scales: Predictions of TDDFT. *J. Chem. Theory Comput.* **11**, 4870–4874 (2015).
36. Töws, W. & Pastor, G. M. Many-body theory of ultrafast demagnetization and angular momentum transfer in ferromagnetic transition metals. *Phys. Rev. Lett.* **115**, 1–6 (2015).
37. Siegrist, F. et al. Light-wave dynamic control of magnetism. *Nature* **571**, 240–244 (2019).
38. Zhang, W. et al. Ultrafast terahertz magnetometry. *Nat. Commun.* **11**, 4247 (2020).
39. Dewhurst, J. K., Elliott, P., Shallcross, S., Gross, E. K. U. & Sharma, S. Laser-induced intersite spin transfer. *Nano Lett.* **18**, 1842–1848 (2018).
40. Hofherr, M. et al. Ultrafast optically induced spin transfer in ferromagnetic alloys. *Sci. Adv.* **6**, eaay8717 (2020).
41. Koshibae, W., Furukawa, N. & Nagaosa, N. Real-time quantum dynamics of interacting electrons: Self-organized nanoscale structure in a spin-electron coupled system. *Phys. Rev. Lett.* **103**, 266402 (2009).
42. Ono, A. & Ishihara, S. Double-exchange interaction in optically induced nonequilibrium state: A conversion from ferromagnetic to antiferromagnetic structure. *Phys. Rev. Lett.* **119**, 207202 (2017).
43. Ono, A. & Ishihara, S. Photoinduced topological spin texture in a metallic ferromagnet. *J. Phys. Soc. Jpn.* **88**, 023703 (2019).
44. Chen, Z. & Wang, L.-w Role of initial magnetic disorder: A time-dependent ab initio study of ultrafast demagnetization mechanisms. *Sci. Adv.* **5**, eaau8000 (2019).
45. Kundu, A. & Zhang, S. Dzyaloshinskii–Moriya interaction mediated by spin-polarized band with Rashba spin–orbit coupling. *Phys. Rev. B* **92**, 094434 (2015).
46. Ado, I. A., Qaiumzadeh, A., Duine, R. A., Brataas, A. & Titov, M. Asymmetric and symmetric exchange in a generalized 2D Rashba ferromagnet. *Phys. Rev. Lett.* **121**, 086802 (2018).
47. Vaishnav, J. & Clark, C. Observing Zitterbewegung with ultracold atoms. *Phys. Rev. Lett.* **100**, 153002 (2008).
48. Liu, X.-J., Borunda, M. F., Liu, X. & Sinova, J. Effect of induced spin–orbit coupling for atoms via laser fields. *Phys. Rev. Lett.* **102**, 046402 (2009).
49. Wu, Z. et al. Realization of two-dimensional spin–orbit coupling for Bose–Einstein condensates. *Science* **354**, 83–88 (2016).
50. Koralek, J. D. et al. Emergence of the persistent spin helix in semiconductor quantum wells. *Nature* **458**, 610–613 (2009).
51. Yang, H. et al. Significant Dzyaloshinskii–Moriya interaction at graphene-ferromagnet interfaces due to the Rashba effect. *Nat. Mater.* **17**, 605–609 (2018).
52. Müller, G. P. et al. Spirit: Multifunctional framework for atomistic spin simulations. *Phys. Rev. B* **99**, 224414 (2019).
53. Atxitia, U., Chubykalo-Fesenko, O., Walowski, J., Mann, A. & Münzenberg, M. Evidence for thermal mechanisms in laser-induced femtosecond spin dynamics. *Phys. Rev. B* **81**, 174401 (2010).
54. Chimata, R., Bergman, A., Bergqvist, L., Sanyal, B. & Eriksson, O. Microscopic model for ultrafast remagnetization dynamics. *Phys. Rev. Lett.* **109**, 157201 (2012).
55. Rybakov, F. N. et al. Magnetic hopfions in solids. Unpublished. Preprint at https://arxiv.org/abs/1904.00250 (2019).
56. Petrović, M. D., Popescu, B. S., Bajpai, U., Plecháč, P. & Nikolić, B. K. Spin and charge pumping by a steady or pulse-current-driven magnetic domain wall: A self-consistent multiscale time-dependent quantum-classical hybrid approach. *Phys. Rev. Appl.* **10**, 054038 (2018).
57. Suresh, A., Bajpai, U. & Nikolić, B. K. Magnon-driven chiral charge and spin pumping and electron-magnon scattering from time-dependent quantum transport combined with classical atomistic spin dynamics. *Phys. Rev. B* **101**, 214412 (2020).
58. Aoki, H. et al. Nonequilibrium dynamical mean-field theory and its applications. *Rev. Mod. Phys.* **86**, 779–837 (2014).
59. Fotso, H. F. & Freericks, J. K. Characterizing the non-equilibrium dynamics of field-driven correlated quantum systems. *Front. Phys.* **8**, 324 (2020).
60. Ikeda, T. N. & Sato, M. General description for nonequilibrium steady states in periodically driven dissipative quantum systems. *Sci. Adv.* **6**, eabb4019 (2020).
61. Karakurt, S., Chantrell, R. & Nowak, U. A model of damping due to spin–lattice interaction. *J. Magn. Magn. Mater.* **316**, e280–e282 (2007).
62. Thonig, D. & Henk, J. Gilbert damping tensor within the breathing fermi surface model: Anisotropy and non-locality. *N. J. Phys.* **16**, 013032 (2014).

Acknowledgements

We thank Nikolai Kiselev, Filipe Guimarães, Manuel dos Santos Dias and Samir Lounis for discussions. We acknowledge financial support from Leibniz Collaborative Excellence project OptiSPIN—Optical Control of Nanoscale Spin Textures. We acknowledge funding under SPP 2137 "Skyrmionics" of the DFG. We gratefully acknowledge financial support from the European Research Council (ERC) under the European Union's Horizon 2020 research and innovation programme (Grant No. 856538, project "3D MAGiC"). The work was also supported also by the Deutsche Forschungsgemeinschaft (DFG, German Research Foundation)—TRR 173/2—268565370 (projects A11 and B12), TRR 288—422213477 (projects B06 and A09). We also gratefully acknowledge the Jülich Supercomputing Centre and RWTH Aachen University for providing computational resources under project Nos. jiff40 and jpgi11.

Author contributions

Y.M., O.G., and S.B. initiated the project. S.G., F.F., and Y.M. formulated the problem and worked out the methodology. S.G. implemented the method and performed the simulations. Y.M. coordinated the project. All authors discussed the results contributed to the analysis of the data and writing of the manuscript.

Competing interests

The authors declare no competing interests.

Additional information

Supplementary information The online version contains supplementary material available at https://doi.org/10.1038/s42005-022-00840-3.

Correspondence and requests for materials should be addressed to Sumit Ghosh.

Peer review information *Communications Physics* thanks the anonymous reviewers for their contribution to the peer review of this work. Peer reviewer reports are available.

Reprints and permission information is available at http://www.nature.com/reprints

Publisher's note Springer Nature remains neutral with regard to jurisdictional claims in published maps and institutional affiliations.